

Micron-scale modifications of Si surface morphology by pulsed-laser texturing

T. Schwarz-Selinger

*Centre for Interdisciplinary Plasma Science, Max-Planck-Institut für Plasmaphysik, D-85748 Garching, Germany,
and the Frederick Seitz Materials Research Laboratory, University of Illinois, Urbana, Illinois 61801*

David G. Cahill

*Department of Material Science and Engineering and the Frederick Seitz Materials Research Laboratory, University of Illinois,
Urbana, Illinois 61801*

S.-C. Chen,* S.-J. Moon, and C. P. Grigoropoulos

*Department of Mechanical Engineering, University of California, Berkeley, California 94720-1740
(Received 22 February 2001; revised manuscript received 8 June 2001; published 27 September 2001)*

The morphologies of Si surfaces are modified with single, tightly focused nanosecond laser pulses and characterized by atomic force microscopy (AFM). Dimple-shaped features with diameters 1–4 μm and depths 1–300 nm are produced by varying the laser-spot diameter and the peak energy densities F_0 in the range $0.4 < F_0 < 1.3 \text{ J cm}^{-2}$. Greater control of the depth of shallow dimples and quantitative comparison of theory and experiment is enabled by first removing the native oxide of Si with dilute HF acid. We develop approximate analytical solutions for two-dimensional fluid-flow driven by gradients in the surface tension; these solutions provide fundamental insight on how the morphology depends on laser parameters and the thermo-physical properties of the melt and its surface. Quantitative comparisons between theory and experiment are enabled by using numerical simulations of heat flow in one-dimension as inputs to the analytical fluid-flow equations; we find good agreement with AFM data for the dimple shape and depth.

DOI: 10.1103/PhysRevB.64.155323

PACS number(s): 68.03.Cd, 66.20.+d, 65.20.+w, 42.62.–b

I. INTRODUCTION

Micron-scale modifications of NiP_x hard-disk substrates by laser processing was demonstrated nearly 10 years ago.¹ Since that time, the process of “laser zone texturing” has become established as a standard manufacturing tool for controlling friction in the landing zone of the disk. Laser texturing does not rely on material removal—as, for example, is the case for laser drilling or laser ablation—but on hydrodynamic redistribution of the molten region produced by inhomogeneous heating. Temperature gradients at the surface of the melt produce gradients in the surface tension that, in most cases, drive fluid from the hot center of the melt to the cold periphery. A dimple-shaped feature is typically observed after resolidification.^{2,3} Laser texturing is a particularly powerful method for creating subtle changes in morphology with good control over the lateral and vertical dimensions of the surface feature.⁴

Although laser texturing of NiP_x has significant technological relevance, a quantitative understanding of the process is hampered by the lack of key data for the high-temperature thermophysical properties of NiP_x and the complexity of the surface properties of this metastable amorphous alloy. Our study of laser texturing of Si is motivated by the opportunity for greater scientific understanding: most of the thermophysical and surface properties of Si are known and therefore we can more critically confront theory with the results of experiment. Using Si, we can remove the native oxide and produce hydrogen termination of the surface by treatment with hydrofluoric (HF) acid; this surface preparation allows us to isolate the role of desorption of surface contaminants in laser texturing.

We have found that laser texturing provides a convenient and flexible method for modifying the morphology of Si substrates and we are applying laser textured Si wafers in other experiments on the physics of epitaxial crystal growth and mass transport on clean crystal surfaces; laser texturing avoids the contamination and substrate damage that is sometimes produced by lithographic processing and plasma etching. Our analytical model for the dimple shape and depth, see Sec. IV, allows us to quantitatively understand how the geometry of the surface feature is controlled by the lateral distribution of energy density in the focused laser beam.

II. EXPERIMENTAL DETAILS

Our apparatus (at U. Illinois) for laser texturing uses a diode-pumped, passively Q -switched and frequency doubled (532 nm) neodymium yttrium aluminum garnet (Nd:YAG) laser that generates nanosecond pulses [full-width-half-maximum (FWHM) $\approx 1 \text{ ns}$] with a repetition rate of 17 kHz. We select a single pulse from the pulse train with an acousto-optic modulator; only the first-order diffracted beam passes through a first aperture. Our standard configuration uses a $\times 5$ beam expansion that produces a $1/e^2$ intensity radius at the back-focal-plane of the objective lens of $w_0 = 4.1 \text{ mm}$. We truncate this beam with a second aperture of radius $a \approx 1.5 \text{ mm}$ to control the energy density at the surface of the sample. In most cases, the focal length of the objective lens is $f = 10 \text{ mm}$; this combination of beam expansion, truncation, and f produces a $1/e^2$ beam diameter on the surface of $2w \approx 3 \mu\text{m}$. For selected experiments, we use

other combinations of the beam expansion and objective lenses to create laser spots of diameter 1, 2, and 4 μm ; in these cases, the energy of the pulse is attenuated by neutral density filters.

Our samples are commercial p-type Si(001) wafers with a resistivity of 1 $\Omega\text{ cm}$. The samples are mounted on a motorized x-y-z stage that positions the sample relative to the objective lens with a resolution of $\sim 50\text{ nm}$. To facilitate placement of the sample surface at the focal plane of the objective lens, we insert a Fresnel beam splitter in the optical path and focus the light reflected from the sample surface onto a small aperture placed in front of a photodetector; the detector signal is maximized when the sample is at the focus of the objective lens. Adjusting the focus becomes rapidly more critical for tightly focused laser beams because the depth-of-focus d scales with the square of the diameter of the laser spot. For example, if we can tolerate a 5% variation in spot size then $d = \pm 8\ \mu\text{m}$ for a beam diameter of $2w = 4\ \mu\text{m}$ and $d = \pm 0.6\ \mu\text{m}$ for the smallest spot size we have investigated $2w = 1.1\ \mu\text{m}$.

We determine the energy E of an individual laser pulse (typically $\approx 300\text{ nJ}$) by measuring the average power of the laser with a calibrated optical power-meter and dividing by the repetition rate measured with a fast photodetector and spectrum analyzer. For a truncated Gaussian beam incident at the back-focal-plane of an objective lens of focal length f , the energy density $F(r)$ at the focal-plane of the objective lens is⁵

$$F(r) = \frac{2Ek^2}{\pi} \left[\int_0^{a/w_0} \rho \exp(-\rho^2) J_0(kr\rho) d\rho \right]^2, \quad (1)$$

where we have defined a characteristic inverse length $k = 2\pi w_0 / (f\lambda)$, J_0 is the zero-order Bessel function, λ the wavelength, w_0 the $1/e^2$ intensity radius of the Gaussian beam at the back-focal plane and a the radius of the truncation aperture in the back-focal plane. We use Eq. 1 to calculate the peak energy density at the center of the beam $F_0 = F(0)$ and define a $1/e^2$ intensity radius w by the relationship $F(w) = F_0/e^2$.

Equation (1) excludes the effects of lens aberrations. Although we have not quantified the aberrations of the objective lenses used in this study, in most cases light fills only a small fraction of the back-focal-plane aperture of the objective lens and therefore, the diffraction limit described by Eq. (1) should be accurate. Only in the case of the smallest spot size we have investigated, $w_0 = 4.1\text{ mm}$, $f = 10\text{ mm}$, and $a = 4.2\text{ mm} = (\text{N.A.})f$, should aberrations have a significant influence on F_0 and w .

The optical properties of Si are well known but more complex than for a metal such as NiP_x . For crystalline Si, the reflectivity is $R = 0.37$ for $\lambda = 532\text{ nm}$; the absorption coefficient at room temperature^{6,7} is $4\pi k/\lambda \approx 7 \times 10^3\text{ cm}^{-1}$ and increases^{8,9} to $\approx 10^5\text{ cm}^{-1}$ at 850°C . The optical properties of liquid Si ($T_m = 1410^\circ\text{C}$) are metallic: the reflectivity of the liquid¹⁰ is greater than the solid, $R = 0.70$, and the absorption coefficient increases dramatically, $4\pi k/\lambda = 1.2 \times 10^6\text{ cm}^{-1}$.

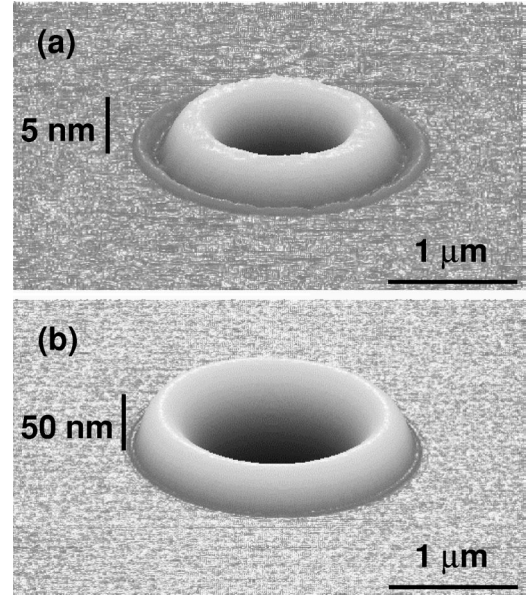


FIG. 1. Three dimensional perspective view of the morphology of typical laser dimples on Si as measured by atomic force microscopy. (a) Peak energy density of the pulse $F_0 = 0.77\text{ J cm}^{-2}$, $1/e^2$ beam diameter $2w = 2.9\ \mu\text{m}$; (b) $F_0 = 1.15\text{ J cm}^{-2}$, $2w = 2.6\ \mu\text{m}$.

All experiments were performed in air. We characterize the dimple shape by atomic force microscopy [(AFM) Digital Instruments Dimension 3100 Series] operating in contact-mode and calibrated with a standard grating.

III. RESULTS AND DISCUSSION

In laser texturing of NiP_x , the shape of the surface feature changes from a shallow dimple, to a sombrero-shape, to a double-rim shape as the energy density is increased.³ These shape changes are thought to be connected to the desorption of surface oxides and possible changes in the alloy composition at the surface; the sombrero-shape in particular gives clear evidence that fluid flows toward the center of the melt, suggesting that the center of the melt has the highest surface tension. By contrast, our investigation reveals that surface features produced by laser texturing of Si keep the same shape over a wide range of energy densities. Figure 1 shows AFM images of typical features. The peak energy density F_0 was varied by changing the truncation of the beam in the back-focal plane of the objective lens, leading to a small decrease of spot size with increasing energy density. A 10% change in the radius a of the truncation aperture changes F_0 by $\approx 40\%$ but produces only a $\approx 10\%$ change in the $1/e^2$ radius w .

In both Figs. 1(a) and 1(b), the shape of the feature can be described as bowl-like crater with a shallow rim raised above the flat Si surface. Increasing F_0 increases both the depth of the crater and the height of the rim. For the feature shown in Fig. 1(a), the distance between the top of the rim and the bottom of the crater is 25 nm; in Fig. 1(b), this distance is 330 nm. We define this length-scale as the “peak-to-peak roughness” of the surface feature. In both images, a secondary, much shallower depression is visible surrounding the

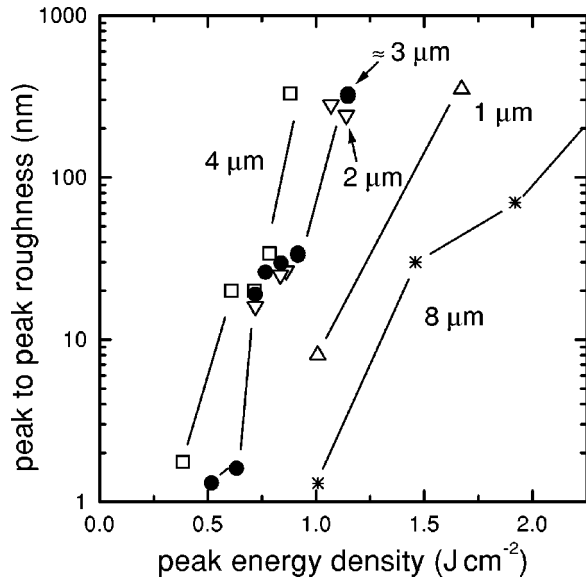


FIG. 2. Influence of the peak energy density of the laser pulse on the peak-to-peak roughness of laser dimples (difference in height between the top of the rim and the bottom of the central crater) for different beam diameters. Each set of data is labeled by the $1/e^2$ beam diameter of the focused optical pulse. Filled circles: energy reduction with beam truncation $2w \approx 3 \mu\text{m}$. Open symbols: energy reduction with absorptive neutral density filters. Stars labeled by $8 \mu\text{m}$ are for comparison and were obtained using a different apparatus (FWHM of 15 ns, frequency doubled Nd:YLF laser).

outer edge of the rim; the depth of that structure, $\approx 1 \text{ nm}$, does not change significantly with F_0 . Integration of the relative height of the feature $\int 2\pi r \Delta z dr$ shows that loss of material by evaporation or ablation is negligible under these conditions.

We used plan-view transmission electron microscopy (TEM) to confirm that the melt-zones recrystallize, as expected, with excellent crystal quality; amorphization of Si wafers by laser melting generally requires the use of nanosecond UV pulses¹¹ to create a temperature gradient and solidification velocity large enough to cause a breakdown in the regrowth of the crystal. The TEM images show, however, a narrow band of contrast, $\approx 50 \text{ nm}$ wide, at the outermost edge of the melt zone. We do not yet understand the nature or origin of the defects responsible for this contrast.

Figure 2 shows the peak-to-peak roughness as a function of energy density at the center of the laser spot F_0 for different values of the $1/e^2$ diameter $2w$. The curves have a striking feature in common: a steep increase when the energy density exceeds a threshold value. From an analysis of the diameters of the outer edge of the effected regions as a function of F_0 , we determine the threshold for melting, $F_{\text{th}} = 0.21 \pm 0.015 \text{ J cm}^{-2}$. Therefore, we observe a significant range of F_0 where the sample melts but the modification of the surface morphology is essentially negligible, $< 2 \text{ nm}$.

For the most tightly focused laser spot, $2w = 1.1 \mu\text{m}$, the curve for the peak-to-peak roughness is shifted to higher values of F_0 . We offer two possible explanations of this behavior: (i) spherical aberrations of the objective lens cause us to overestimate the true value of F_0 based on Eq. (1) and (ii) a

significant amount of heat may be lost to lateral heat conduction in the sample. Both of these mechanisms are probably valid but the morphologies of these small features show a central domelike structure at intermediate energies, suggesting that lens aberrations are indeed playing an important role.

Data for $2w = 8 \mu\text{m}$ are shifted even further to the right on Fig. 2; these data are from a different apparatus (at UC Berkeley) that used an actively Q -switched laser with a much longer pulse width, FWHM $\approx 15 \text{ ns}$. The larger laser spot and longer pulse-width result in smaller temperature gradients at the surface of the melt and a correspondingly smaller peak-to-peak roughness for a given energy density. These data are included for completeness; because of the substantial differences in pulse width and spot size, a direct comparison with the short pulse, small spot size data is difficult.

A typical native oxide of Si has a stoichiometry close to SiO_2 and a thickness of 2–3 nm. The presence of this oxide layer greatly hinders any quantitative comparisons between experiment and theory because we have little knowledge of how changes in the microstructure and desorption of the oxide layer alters the surface tension of the laser melt.¹² For these reasons, we compare laser texturing before and after treatment with hydrofluoric (HF) acid. First, dimples are produced on an untreated Si surface terminated by the native oxide. Subsequently, we pour a 5% solution of HF over the sample and repeat the laser texturing process at a different location on the same Si sample. In this way, we avoid any drift in the laser pulse energy that could produce systematic errors. HF acid is known to remove the native oxide and create a hydrophobic, hydrogen-terminated surface.¹³ We assume that the hydrogen termination desorbs immediately upon laser processing and has little effect on the intrinsic properties of clean Si.

Figure 3 shows the peak-to-peak roughness as function of F_0 for Si samples with the native oxide intact and samples with the oxide removed by the HF treatment described above. The peak-to-peak roughness of HF-treated Si increases more smoothly and reproducibly with F_0 than Si covered by the native oxide: the oxidized sample shows an abrupt increase in roughness at $F_0 > 0.6 \text{ J cm}^{-2}$ and then a plateau for $0.65 < F_0 < 0.9 \text{ J cm}^{-2}$. Because the viscosity of SiO_2 is orders of magnitude larger than the viscosity of liquid Si, we do not envision thermocapillary flow of the oxide itself; rather, we attribute the differences between the oxidized and HF treated samples to surface tension gradients created by the break-up and desorption of the oxide layer at $F_0 > 0.6 \text{ J cm}^{-2}$.

In addition to these differences in total roughness, a subtle but distinctive difference in the morphology is found across the entire range of F_0 : oxidized samples show a small ($\approx 1 \text{ nm}$ tall) rim at the outer edge of the melt zone—see, for example, Fig. 1(a)—but HF-treated Si shows a narrow groove $\approx 1 \text{ nm}$ deep. We make a quantitative comparison in Fig. 4 where we plot AFM line scans through the center of surface features created at values of F_0 relatively close to the threshold for melting. We do not yet understand the origin of these small features at the edge of the melt zone, although lateral solidification at the edge of the melt may contribute.

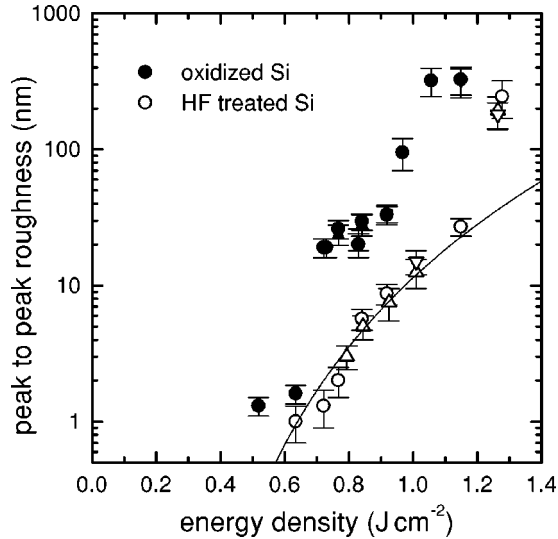


FIG. 3. Peak to peak roughness of the dimples measured with AFM as a function of surface condition. Filled symbols: surface covered by a typical native oxide of Si; open symbols: surface treated by dilute HF acid prior to laser texturing. In both cases, $2w \approx 3 \mu\text{m}$. The solid line is a fit to the data for HF-treated Si using the functional form $\Delta z = C(F_0 - F_{\text{th}})^4$, where F_{th} is the threshold for melting, determined independently, and the constant C is adjusted to fit the data; $C = 30 \text{ nm cm}^8 \text{ J}^{-4}$.

Figure 4 also demonstrates a second difference in morphology that exists only near the threshold for melting. At these low values of F_0 , the surface curvature at the center of the feature is positive for HF-treated Si, as expected for thermocapillary flow of a liquid with a clean surface, but negative for an oxidized Si sample. Apparently, at energy densities near the threshold for melting, changes in the stress or microstructure of the native oxide layer are sufficient to cause a subtle fluid flow toward the center of the laser spot.

IV. MODEL FOR THE DIMPLE SHAPE AND DEPTH

To gain insight on the dimple-shape and the strong dependence of the depth of the dimples on the energy density of the laser pulse, we develop below approximate analytical solutions to the equations of fluid flow in the melt that determine the final morphology. Our goal is to use one-dimensional calculations of surface temperature T_s and melt depth h during laser processing, e.g., as provided by Wood and co-workers,^{14,15} to predict two-dimensional fluid flow driven by the inhomogeneous T_s distribution created by a tightly focused laser beam.

A. Limit of a long laser pulse

We first consider the limit when the time scale of the laser pulse Δt is large compared to the time scale for the diffusion of fluid momentum through the thickness of the melt, i.e., $\Delta t \gg h^2/\nu$, where h is the melt depth, and ν the kinematic viscosity. We choose cylindrical coordinates: the origin of the coordinate system is located at the surface of the sample (before the formation of the dimple) and at the center of the laser spot; r is the radial coordinate and the sample is $z < 0$.

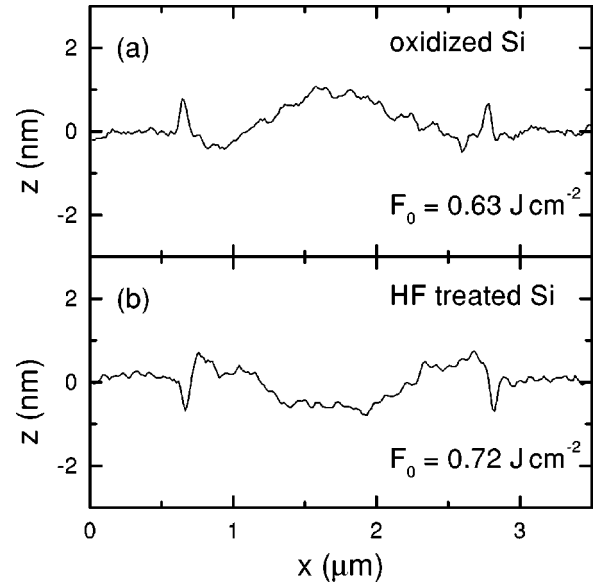


FIG. 4. Line scans of the morphology of Si laser dimples, as measured by AFM, at energies near the threshold for melting: (a) Si terminated by native oxide; (b) Si surface treated by dilute HF acid prior to laser texturing.

For an incompressible, steady-state flow in the limit of large viscosity, the continuity equation and the Navier-Stokes equation for the fluid velocity \vec{v} reduce to¹⁶

$$\vec{\nabla} \cdot \vec{v} = 0, \quad \nabla^2 \vec{v} = 0. \quad (2)$$

The boundary conditions on \vec{v} are (i) that the fluid flow vanishes at the bottom of the melt, $\vec{v} = 0$ at $z = -h$ and (ii) at the surface, $z = 0$,

$$\eta \left(\frac{\partial v_r}{\partial z} + \frac{\partial v_z}{\partial r} \right) = \frac{\partial \alpha}{\partial r}, \quad (3)$$

where α is the surface tension, η the dynamic viscosity of the fluid, and the subscripts r and z label the radial and normal components of the velocity, respectively.

To make progress in solving these equations, we assume that the melt is shallow; i.e., we assume that derivatives with respect to z are large compared to derivatives with respect to r . The Navier-Stokes equation then simplifies to two scalar equations of motion

$$\frac{\partial^2 v_r}{\partial z^2} = 0, \quad \frac{\partial^2 v_z}{\partial z^2} = 0. \quad (4)$$

Integrating the first of these equations twice gives the radial component of the velocity as a function of depth.

$$v_r = \frac{1}{\eta} \frac{\partial \alpha}{\partial r} (h + z). \quad (5)$$

With the assumption of constant viscosity η , we insert Eq. (5) into the continuity equation and solve for v_z .

$$v_z = - \int_{-h}^0 \frac{1}{r} \frac{\partial}{\partial r} (r v_r) dz \quad (6)$$

$$= \frac{1}{2\eta r} \frac{\partial}{\partial r} \left(r h^2 \frac{\partial \alpha}{\partial r} \right). \quad (7)$$

The problem now reduces to the problem of finding the dependence of the surface tension α and the melt depth h on the radial coordinate r . For clean surfaces of simple materials, $\partial\alpha/\partial T$ is often a constant independent of T ; therefore,

$$\frac{\partial \alpha}{\partial r} = \frac{\partial \alpha}{\partial T} \frac{\partial T_s}{\partial r}, \quad (8)$$

where we have added the subscript s to emphasize that T_s is the temperature at the surface of the melt.

The change in the morphology of the fluid Δz is the integral of v_z over time. Since the temperature excursion $T_s(t)$ is more strongly peaked as a function of time than the melt depth $h(t)$, we define an integrated temperature I and an average melt depth $\langle h^2 \rangle$.

$$I = \int_{T_s > T_m} (T_s - T_m) dt, \quad (9)$$

$$\langle h^2 \rangle I = \int_{T_s > T_m} h^2 (T_s - T_m) dt, \quad (10)$$

where the integrals are over the lifetime of the melt, i.e., when the surface temperature T_s exceeds the melting temperature T_m . Finally, we have the desired equation describing the change in the morphology produced by the laser pulse.

$$\Delta z = - \frac{1}{2\eta r} \frac{\partial \alpha}{\partial T} \frac{\partial}{\partial r} \left(r \langle h^2 \rangle \frac{\partial I}{\partial r} \right). \quad (11)$$

B. Limit of a short laser pulse

Next, we examine an approximate solution for the limit of a short laser pulse; i.e., a laser pulse length Δt such that $\Delta t \ll h^2/\nu^2$. We assume that the radial momentum in the fluid produced by the surface tension gradients is conserved for short times and that the momentum decays exponentially with a rate $\gamma = 2\nu/h^2$. We write the radial component of the velocity v_r as

$$v_r = \phi \exp(-\gamma t), \quad (12)$$

where the function ϕ satisfies the following expression of momentum conservation:

$$\rho \int \phi dz = \int \frac{\partial \alpha}{\partial r} dt. \quad (13)$$

[The exact solution¹⁷ for a fixed melt depth h has a slightly faster decay-rate at long times, $\gamma = \pi^2\nu/(4h^2)$, but we have verified that our approximate solution gives the correct result for the integrals of v_r over t and z .]

As before, we insert v_r in the continuity equation, solve for v_z and integrate over time to get the change in morphology:

$$\Delta z = \int \int \frac{1}{r} \frac{\partial}{\partial r} [r \phi \exp(-\gamma t)] dz dt. \quad (14)$$

Combining this expression with Eqs. (9), (13), and $\eta = \rho\nu$ yields the same final equation for the morphology as we obtained for the limit of a long laser pulse, Eq. (11), but with a different definition of the average of the square of the melt depth $\langle h^2 \rangle$,

$$\langle h^2 \rangle = 2\nu \int_0^\infty \exp(-2\nu t/h^2) dt. \quad (15)$$

C. Comparison of theory and experiment

Dimensional analysis of Eq. (11) reveals immediately why the peak-to-peak roughness increases abruptly with increasing energy density F . Much of the energy of the optical pulses is absorbed by the latent heat of melting L ; therefore, $h \sim (1-R)(F-F_{\text{th}})/L$ where F_{th} is the threshold energy density for melting, and R is the optical reflectivity of the melt. Similarly, the temperature excursion is mostly controlled by the melt depth and the thermal conductivity of the liquid Λ ; therefore $I \sim (1-R)(F-F_{\text{th}})h/\Lambda$. We replace differentials of r by the radius of the laser spot w and obtain

$$\Delta z \sim (1-R)^4 \frac{\partial \alpha}{\partial T} \frac{(F-F_{\text{th}})^4}{\eta L^3 \Lambda w^2}. \quad (16)$$

A fit to the data for HF-treated Si of the form $\Delta z = C(F-F_{\text{th}})^4$ is plotted on Fig. 3; the predicted dependence agrees well with the data.

A more complete and quantitative comparison of theory and experiment requires knowledge of $I(r)$ and $\langle h^2(r) \rangle$. We assume that lateral heat flow is negligible and, therefore, the dependence of I and $\langle h^2 \rangle$ on the radial coordinate r is given exclusively by the radial distribution of the energy density $F(r)$ according to Eq. (1). We calculate the time evolution of the surface temperature and melt depth for various values of F using one-dimensional numerical simulations of optical absorption and heat conduction, following the work of Refs. 14 and 15. These numerical data for $T(t)$ and $h(t)$ are then integrated [according to Eq. (9) and either Eq. (10) or Eq. (15)] to give $I(F)$ and $\langle h^2(F) \rangle$, see Fig. 5. With $h \approx 100$ nm, $\nu = 2.4 \times 10^{-7}$ m² s⁻¹, $h^2/(2\nu) \approx 20$ ns and we choose the short-pulse limit for calculating $\langle h^2 \rangle$. Finally, we use these results of our computational work as inputs and numerically evaluate the analytical solution for the morphology, Eq. (11).

Figure 6 shows a comparison of the measured topography with a numerical solution of Eq. (11). We have adjusted only one parameter, the peak energy density F_0 , to improve the fit to the data—the best fit uses $F_0 = 0.82$ J cm⁻², 25% less than the experimental value of $F_0 = 1.1$ J cm⁻². All other inputs to the model are fixed: I and $\langle h^2 \rangle$ are calculated using the known temperature-dependent thermal conductivity, heat

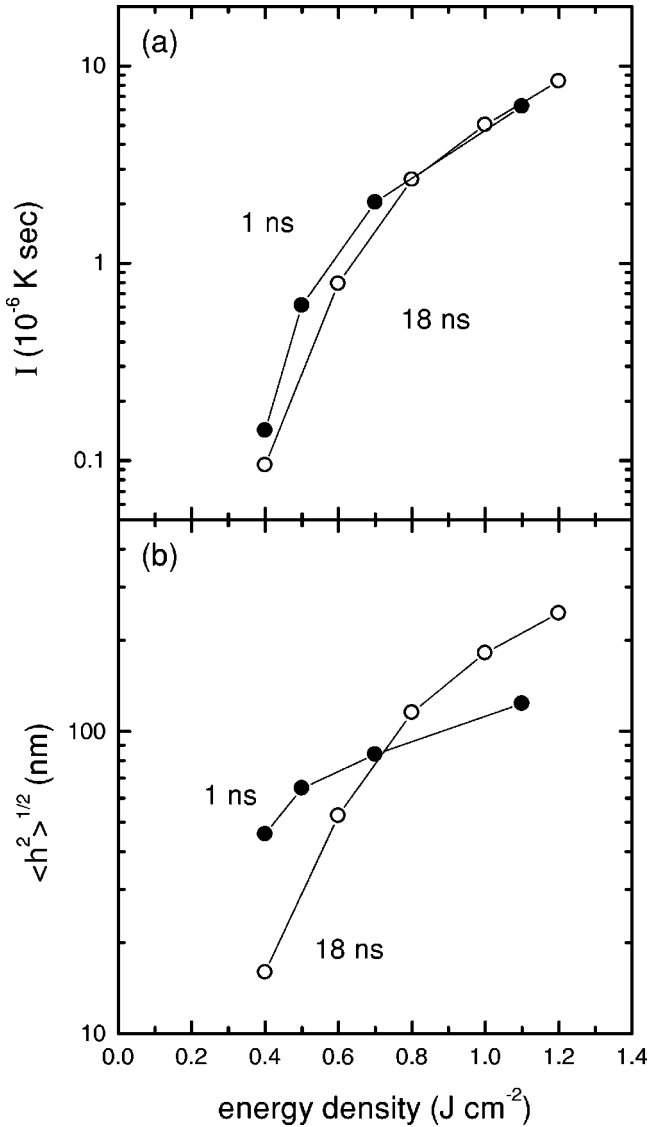


FIG. 5. Filled circles: (a) integrated temperature I [Eq. (9)] and (b) square root of $\langle h^2 \rangle$ [Eq. (15)] for FWHM=1 ns, $\lambda=532$ nm, optical pulses calculated from one-dimensional numerical simulations of optical absorption and heat transfer in Si and plotted as a function of the energy density F of the pulse. Open circles are included for comparison: (a) I [Eq. (9)] and (b) square root of $\langle h^2 \rangle$ [Eq. (10)] for FWHM=18 ns, $\lambda=532$ nm, optical pulses calculated from the numerical results published in Ref. 15.

capacity, and optical properties of Si;¹⁵ the temperature coefficient of the surface tension¹⁸ is $\partial\alpha/\partial T = -7.4 \times 10^{-5}$ N m⁻¹ K⁻¹ and the viscosity of liquid Si (Ref. 19) is $\eta = 6 \times 10^{-4}$ Pa s. The agreement between the data and the prediction of Eq. (11) is good, particularly given the substantial approximations required in the derivation of Eqs. (11) and (15).

We have ignored capillarity: the product of the surface tension and the surface curvature provides a driving force for restoring the morphology of the melt to a flat surface. For a shallow capillary wave, the dispersion relationship is $\rho\omega^2 = \alpha hk^4$, where $k = 2\pi/\lambda$ is the wave number. To evaluate the relaxation rate of the morphology due to capillarity, we compare the damping coefficient $\gamma = 2\nu/h^2$ to ω .

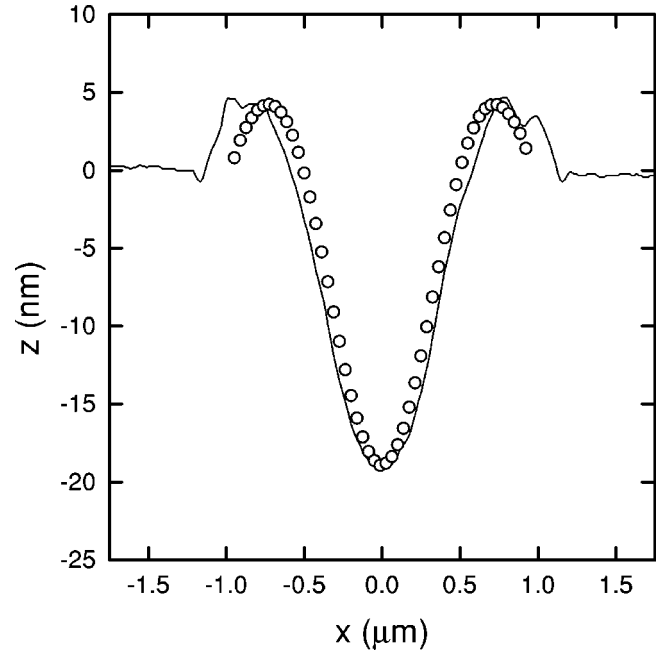


FIG. 6. Comparison of the morphology of a laser dimple ($F_0 = 1.1$ J cm⁻², $2w = 2.6$ μ m) created on HF treated Si as measured by AFM (solid line) and predicted (open circles) by Eq. (11) using the 1 ns data for I and $\langle h^2 \rangle$ shown in Fig. 5, $F(r)$ calculated with Eq. (1), and $F_0 = 0.82$ J cm⁻².

$$\frac{\gamma}{\omega} = \frac{2\eta}{\sqrt{\rho\alpha h}} \frac{1}{(kh)^2}. \quad (17)$$

Typical values of the geometrical factors are $k = 3 \times 10^6$ m⁻¹ and $h = 150$ nm; evaluating Eq. (17) with the properties of Si^{20,18} ($\rho = 2.5 \times 10^3$ kg m⁻³, $\alpha = 0.73$ J m⁻²) we find $\gamma/\omega \approx 0.5$ and capillary waves are underdamped in the geometry of our experiment. We can then use $1/\omega$ to estimate the time scale of this relaxation: $1/\omega \approx 20$ ns. This time scale is comparable to the melt time and we conclude that capillarity may play some role in determining the final morphology. Oxidation of the liquid Si surface following the laser pulse could increase the damping coefficient considerably and greatly decrease the relaxation rate due to capillarity. This enhanced damping of a capillary wave by an adsorbed film is discussed in a problem in Landau and Lifshitz.¹⁶

ACKNOWLEDGMENTS

This work was supported by NSF Grant No. CTS 99-78822 and the U.S. Department of Energy, Division of Materials Sciences under Award No. DEFG02-ER9645439, through the Frederick Seitz Materials Research Laboratory at the University of Illinois at Urbana-Champaign. Characterization of surface morphologies by atomic force microscopy and microstructure by transmission electron microscopy used the facilities of the Center for Microanalysis of Materials, University of Illinois.

*Present address: Industrial and Manufacturing Systems Engineering Department, 2019 Black Engineering, Iowa State University, Iowa 50011.

- ¹R. Ranjan, D.N. Lambeth, M. Tromel, P. Goglia, and Y. Li, *J. Appl. Phys.* **69**, 5745 (1991).
- ²T.D. Bennett, D.J. Krajnovich, C.P. Grigoropoulos, P. Baumgart, and A.C. Tam, *J. Heat Transfer* **119**, 589 (1997).
- ³S.C. Chen, D.G. Cahill, and C.P. Grigoropoulos, *J. Heat Transfer* **122**, 107 (2000).
- ⁴H.K. Park, P.J.M. Kerstens, P. Baumgart, and A.C. Tam, *IEE Trans. Magn.* **34**, 1807 (1998).
- ⁵Miles V. Klein and Thomas E. Furtak, *Optics*, 2nd ed. (Wiley, New York, 1986), see Chap. 6, and, in particular, p. 359.
- ⁶G.E. Jellison and F.A. Modine, *J. Appl. Phys.* **53**, 3745 (1982).
- ⁷D.E. Aspnes, in *Properties of Crystalline Silicon*, 2nd ed., edited by R. Hull (IEE Publishing, Edison, NJ, 1999), Chap. 12.2, pp. 683–690.
- ⁸Byung K. Sun, Xiang Zhang, and Costas P. Grigoropoulos, *Int. J. Heat Mass Transf.* **40**, 1591 (1997).
- ⁹J. Šik, J. Hora, and J. Humlíček, *J. Appl. Phys.* **84**, 6291 (1998).
- ¹⁰D.E. Aspnes, in *Properties of Crystalline Silicon*, 2nd ed., edited by R. Hull (IEE Publishing, Edison, NJ, 1999), Chap. 12.4, p. 696.
- ¹¹J.A. Yater and Michael O. Thompson, *Phys. Rev. Lett.* **63**, 2088 (1989).
- ¹²V.Y. Balandin, D. Otte, and O. Bostanjoglo, *J. Appl. Phys.* **78**, 2037 (1995).
- ¹³E. Yablonovitch, D.L. Allara, C.C. Chang, T. Gmitter, and T.B. Bright, *Phys. Rev. Lett.* **57**, 249 (1986).
- ¹⁴R.F. Wood and G.E. Giles, *Phys. Rev. B* **23**, 2923 (1981).
- ¹⁵R.F. Wood and G.E. Jellison, Jr., in *Semiconductors and Semimetals*, edited by R.F. Wood, C.W. White, and R.T. Young (Academic Press, Orlando, 1984), Vol. 23, Chap. 4, pp. 165–250.
- ¹⁶L.D. Landau and E.M. Lifshitz, *Fluid Mechanics* (Pergamon Press, London, 1959), see Chap. II; for a discussion of damping of fluid motion by an adsorbed film, see p. 241.
- ¹⁷H.S. Carslaw and J.C. Jaeger, *Conduction of Heat in Solids*, 2nd ed. (Oxford University Press, New York, 1995), see p. 359.
- ¹⁸H. Fujii, T. Matsumoto, N. Hata, T. Nakano, M. Kohno, and K. Nogi, *Metall. Mater. Trans. A* **31**, 1585 (2000).
- ¹⁹Yuzuru Sato, Takefumi Nishizuka, Tomohiro Tachikawa, Masayoshi Hoshi, Tsutomu Yamamura, and Yoshio Waseda, *High Temp.-High Press.* **32**, 253 (2000).
- ²⁰Mario Langen, Taketoshi Hibiya, Minoru Eguchi, and Ivan Egry, *J. Cryst. Growth* **186**, 550 (1998).